LIGHTWEIGHT RESEARCH OF FORESTRY UNMANNED VEHICLE SWING ARMS BASED ON MULTI-CONDITION TOPOLOGY OPTIMIZATION OF CONTINUUM STRUCTURES
/
基于连续体结构多工况拓扑优化的林业无人车辆摆臂轻量化研究

Yihan QIN, Yilu ZHAO, Qiang CHEN, Ji WU, Zhongjia CHEN, Qingchun WANG, Xiangyue YUAN*)
The School of Technology, Beijing Forestry University, Beijing / China
Tel: +086-13366903021; E-mail: yuanxiangyue@bjfu.edu.cn
Corresponding author: Xiangyue Yuan
DOI: https://doi.org/10.35633/inmateh-76-91

Keywords: *Dynamics Simulation; Structure Optimization; Finite Element Analysis; Modal Test*

ABSTRACT
To meet the demanding terrain of China's forest regions—characterized by obstacles, gullies, and uneven ground—a wheel-leg hybrid chassis is proposed for a three-axle unmanned electric forestry vehicle. Parametric modelling in SolidWorks and dynamic simulations in MSC Adams quantified the critical load cases on the swing arms during obstacle negotiation. The Analytic Hierarchy Process (AHP) assigned optimal weights for multi-scenario topology optimization. A finite-element model of the arms was built in HyperMesh/OptiStruct; post-optimisation analyses confirmed structural integrity. Masses of the front and rear arms reduced to 31.3 kg each, and the middle arm to 39.44 kg, realizing weight reductions of 29.1 % and 21.7 %, respectively, with no loss in performance.

摘要
为应对中国大陆林区存在众多障碍物和沟壑等林业作业条件所带来的挑战，本文提出了一种适用于林业三轴无人电动车辆的轮腿式混合行走机构。利用 SolidWorks 和 MSC Adams 软件进行了参数化建模和动力学仿真，以分析车辆摆臂在越障过程中所经历的多种典型载荷工况，运用层次分析法（AHP）确定了多工况拓扑优化的最优权重系数分配。使用 Hypermesh-Optistruct 软件建立了摆臂的有限元模型，并对优化后的摆臂进行了有限元分析。优化后的前、后摆臂重量均为 31.3 千克，中摆臂重量为 39.44 千克，重量分别降低了 29.1%和 21.7%，取得了良好的轻量化效果。

INTRODUCTION
Currently, forest engineering vehicles in China face the challenge of off-road capabilities when operating in forested areas. The operating environment in forest regions is more complex and difficult than ordinary environments. Since forestry production vehicles often need to operate on non-structured terrains in the forest, ordinary wheeled or tracked vehicles struggle to meet the obstacle-crossing performance requirements in complex site conditions, such as numerous ravines and vertical obstacles (*Sun et al., 2019*). This paper, based on a 6×6 wheel-hub motor driven, tri-axle electric unmanned vehicle, studies a walking mechanism that integrates strong obstacle-crossing capabilities, combining the advantages of wheeled vehicles for high-speed travel and legged structures for superior terrain adaptability. This mechanism is designed to meet the random changes in forest terrain and road conditions.

Chen et al. proposed a structural optimization scheme for tree transplanters designed for hilly and mountainous environments to enhance their stability and maneuverability during climbing, obstacle crossing, and trench crossing. Simulation and real-vehicle testing, conducted using the RecurDyn V9R4 dynamic analysis software, demonstrated that the design meets driving performance requirements (*Chen et al., 2024*). Mergl et al. studied the performance of a hydraulic harvester crane operating on slopes with varying inclines and investigated the impact of slewing bearing angles on slewing torque using MSC Adams simulations (*Mergl & Kašpárek, 2022*).

Wang et al. proposed a passive morphing wheel-legged robot design for obstacle crossing. Kinematic simulations of the robot's morphing and obstacle-crossing processes were conducted using MSC Adams, and the design's feasibility was validated through physical prototype experiments (*Wang Y. et al., 2024*). *Zhou, Liu at al.* have utilized Adams software for kinematic and dynamic analyses of mechanisms, studying both their dynamic and static characteristics (*Huaitang et al., 2024; Liu, 2020*). Chen et al. developed an independent strut-type air suspension system for high-clearance self-propelled sprayers, employing HyperMesh for finite element analysis of critical components like vertical shafts and steering arms. Their design achieved effective vibration damping through air spring optimization and additional air chamber damping, demonstrating a 20-inch vibration reduction stroke while maintaining structural integrity under extreme conditions such as side slip and emergency braking (*Chenwei et al., 2023*). *Wentao et al.* proposed a novel high-clearance chassis design for weeding robots featuring cross-floating suspension mechanisms. Through dynamic simulations and field tests, they achieved 800 mm ground clearance with 22° longitudinal and 32° transverse slope stability, while maintaining structural integrity under 134.88 MPa stress during emergency braking conditions through optimized beam connections *(Wentao et al., 2025*).

The swing arm of a tri-axle unmanned vehicle, as a critical component of the drive system, primarily absorbs impact forces from the ground when driving on complex terrain and overcoming vertical obstacles. Therefore, the structural strength and stiffness of the swing arm are key technical indicators in the design process. Lightweight design, while ensuring the structural strength of the swing arm, can reduce the resistance from the ground, enhance obstacle-crossing performance on challenging terrain, and improve the battery life of an electric vehicle. This ultimately increases their practical application value in forestry operations. With the rapid advancement of optimization algorithms, continuum structure topology optimization has gradually become one of the main approaches to achieving lightweight structural design (*Qiang et al., 2024*).

Wang et al. proposed an improved Solid Isotropic Material with Penalization (SIMP) method and introduced a sensitivity filtering method based on Gaussian weighting functions. The new topology optimization method has advantages such as faster convergence speed and suppression of grayscale elements (*Jing-liang et al., 2022*). Meng et al. applied fuzzy and probabilistic theory to handle cognitive and stochastic uncertainties and studied the flexibility reliability optimization of continuum structures (*Meng et al., 2020*). *Li et al.* proposed a topology optimization method for continuum structures under stress constraints with non-periodic loads, based on the Bidirectional Evolutionary Structural Optimization (BESO) method, which is suitable for dynamic stress under non-periodic loads with iterative periodic updates (*Li et al., 2023*). *Xia et al.* established a non-probabilistic reliability topology optimization model considering local strength characteristics of structures, based on stress influence functions (*Xia & Qiu, 2022*). *Xiaokai et al.* proposed a multi-material topology optimization method for shell/fill structures for automotive control arms, establishing a material interpolation model to achieve better lightweighting results (*Xiaokai et al., 2021*). *Zhang, Wang et al.* developed an integrated lightweight method for steel-aluminum hybrid materials based on sensitivity analysis, reducing the cabin mass by 12.8% and the frame mass by 5.6% (*Wang C. et al., 2024; Zhang et al., 2020*). *Xiong et al.* employed a multi-objective particle swarm optimization algorithm to reduce the weight of the body-in-white by 4.12 kg while ensuring other mechanical properties *(Xiong et al., 2018*). In recent years, many researchers have introduced deep learning models into the topology optimization process, using initial iterative structural density distributions and gradient values as starting information to quickly obtain reliable topological configurations, thereby improving the efficiency of topology optimization (*Padhi et al., 2024; Qiu et al., 2021*).

In summary, this paper focuses on the lightweight design and vertical obstacle-crossing performance of a tri-axle unmanned vehicle. It conducts a vehicle dynamic simulation, with the swing arm as the research object, to analyze the force conditions under various operating conditions. Subsequently, a multi-condition topology optimization design is performed, and a finite element model of the swing arm is established to analyze and verify the performance of the optimized structure (*Kešner et al., 2021; Niu et al., 2022*). A test bench for the swing arm is built to conduct static analysis and modal analysis on the swing arm specimens. The calculated results are compared with experimental data to validate the effectiveness of the topology optimization model and the accuracy of the finite element analysis (*Zhao et al., 2025*).

MATERIALS AND METHODS

Structure Composition and Dynamic Simulation

The structure of the unmanned vehicle consists of three pairs of symmetrically arranged deformable swing arms and a frame-type vehicle body. The drive electric cylinders, hinged to the vehicle body, control the swing arm angles to switch between the wheeled mode and the legged mode, thus achieving the objectives of off-road and vertical obstacle-crossing. For the specific condition of vertical obstacle-crossing, the vehicle needs to smoothly cross a high platform with a maximum height of 1 meter. A simplified dynamic model of the entire vehicle will be established and simulated in the MSC Adams for analysis.

Establishment of the Vehicle Dynamic Simulation Model

The simplified dynamic model after importing is shown in Fig 1, with the main components including the vehicle frame, drive electric cylinders and piston rods, tri-axle swing arms, and wheels. According to the preliminary design requirements, the total mass of the vehicle frame, swing arms, arm drive devices, and related components should be kept within 745 kg, with the mass of a single swing arm not exceeding 42 kg. Considering that modules such as batteries, perception systems, and auxiliary power systems also need to be installed on the vehicle frame, the frame in the model is defined as 1650 kg, and the total weight of the unmanned vehicle is controlled at around 2650 kg, with a single swing arm weighing 42 kg. This ensures the accuracy of the simulation results. The vehicle dimensions and weight parameters are shown in Table 1.

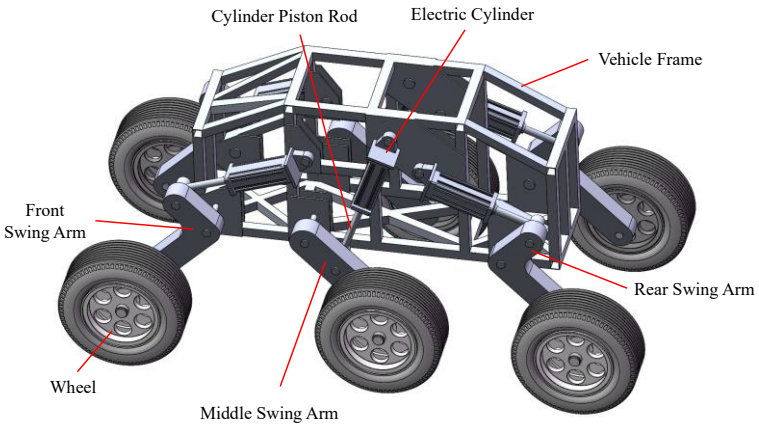

Fig. 1 - The simplified dynamic model of the vehicle

Table 1

The parameters of the vehicle model

Parameter	Value
Vehicle Dimensions(mm)	4130 × 1970 × 1960
Vehicle Weight(kg)	2650
Vehicle Frame Weight(kg)	1650
Single Swing Arm Weight(kg)	42
Single Drive Cylinder Weight(kg)	30
Single Wheel Weight(kg)	100

Through the simulation, the main connections in the unmanned vehicle's dynamic model are as follows:

1. A rotational joint between the lower end of the swing arm and the wheel;
2. A rotational joint between the middle of the swing arm and the vehicle frame;
3. A rotational joint between the upper end of the swing arm and the electric cylinder's piston rod;
4. A translational joint between the electric cylinder's piston rod and the cylinder body;
5. A rotational joint between the end of the electric cylinder and the vehicle frame.

The contact between the wheels, the ground, and obstacles is added using an im-pact function method, with Coulomb friction between the wheels and the ground. The parameters are shown in Table 2.

Table 2

The parameters of the contact

Parameter	Value
Stiffness(N/mm)	1.0×10^4
Collision index	2.2
Damping(N·s/mm)	10
Penetration depth /mm	0.1
Static friction coefficient	0.8
Dynamic friction coefficient	0.1

Dynamic Simulation Process and Results

During the obstacle-crossing process, due to the relatively heavy weight of the unmanned vehicle, in order to prevent excessive force on the swing arm drive electric cylinders, the wheel drive speed is set to 0.2 m/s, and the obstacle-crossing rotational speed is set to 0.04 m/s. The off-road performance of the entire vehicle is then verified. The simulation results are shown in Fig. 2, with the obstacle-crossing process completed within 200 seconds.

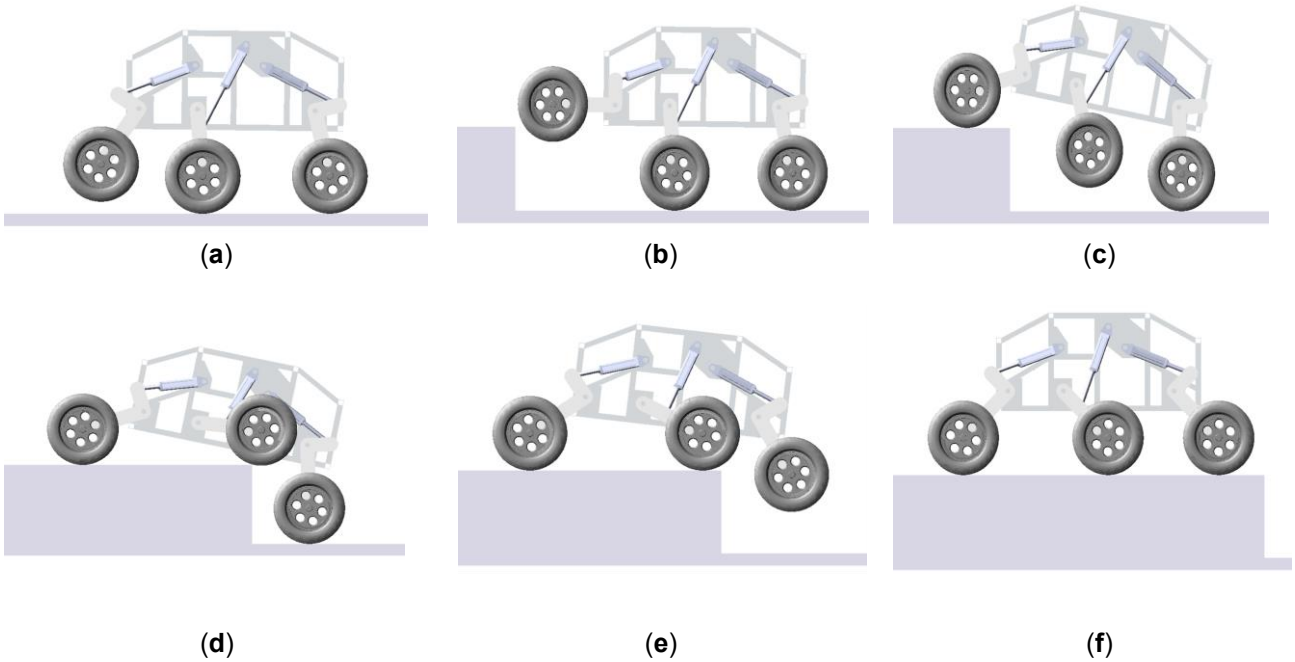

Fig. 2 - The obstacle-crossing process schematic diagram

*(**a**) The middle/rear arm raises to lift the vehicle's posture; (**b**) The front arm is raised to a horizontal angle, approaching the obstacle; (**c**) The front wheel crosses the obstacle while the front arm begins to retract; (**d**) The middle wheel crosses the obstacle while the middle arm begins to retract; (**e**) The middle/rear arm returns to the normal driving angle; (**f**) The vehicle completes the obstacle-crossing.*

In Fig. 3, the gray curve represents the change in the center of mass position of the unmanned vehicle along the vertical direction. This curve indicates that the vehicle maintains overall stability during the wheel-leg transition, wheeled movement, and obstacle-crossing process. The red curve represents the center of mass velocity curve of the vehicle, and the blue curve represents the center of mass acceleration curve. From 0 to 10 seconds, all three-axles swing arms are raised to improve the vehicle's posture, causing the center of mass to rise and resulting in a sudden change in velocity and acceleration. From 10 to 50 seconds, the vehicle approaches the obstacle platform, and its center of mass velocity and acceleration gradually stabilizes. After 50 seconds, the vehicle begins to cross the obstacle and climb the slope, with its center of mass acceleration approaching zero, indicating that its motion is relatively stable.

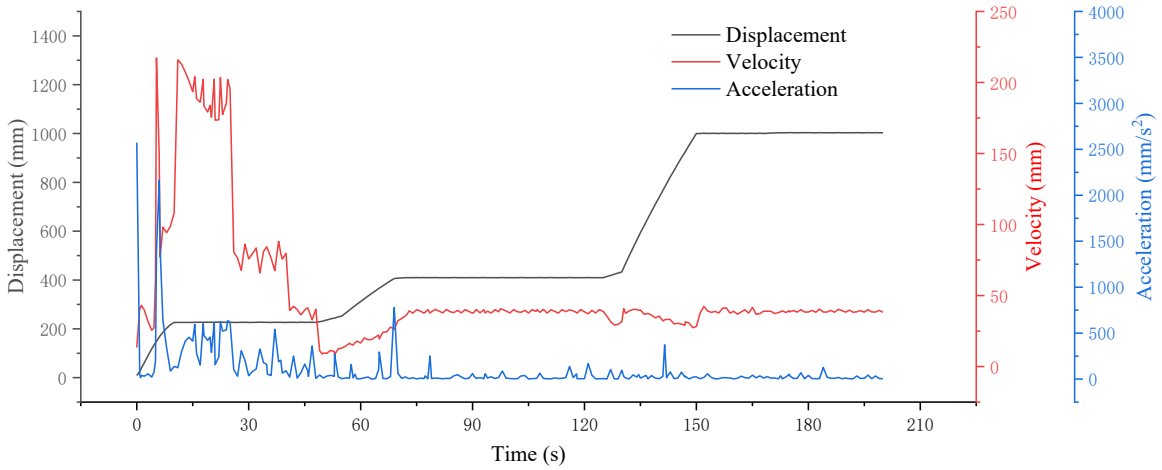

Fig. 3 - The center of mass displacement, velocity, and acceleration curves of the unmanned vehicle during the obstacle-crossing process

The lifting of the swing arm is achieved by controlling the driving cylinder. During the entire obstacle-crossing process, the drive cylinder needs to provide sufficient thrust and pull to enable the wheel-leg transformation of the unmanned vehicle and withstand the impact forces encountered during the obstacle-crossing. Therefore, the force conditions at the connection between each swing arm and the cylinder rod were also studied in Adams software, as shown in Fig. 4, which provides more reference for the subsequent structural topology optimization loading conditions.

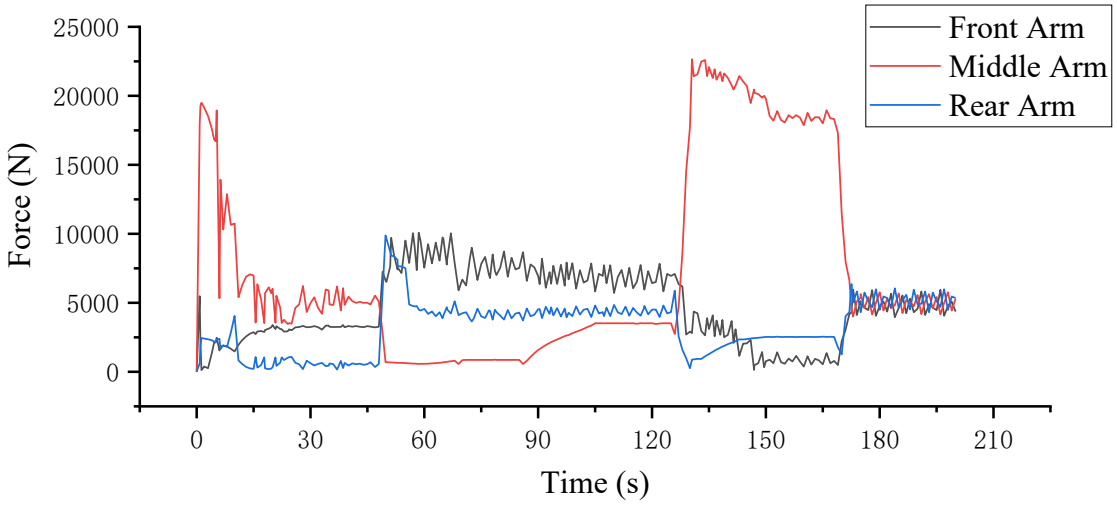

Fig. 4 - Force diagram at the connection between each axle Swing Arm and the Drive Cylinder Rod

From Fig. 4, it can be seen that the force conditions of the front/rear swing arms during the wheel-leg transformation and obstacle-climbing stages are quite similar, and the load they bear is smaller compared to the middle swing arm. Considering the interchangeability of the structure, the front/rear swing arms can be merged in the subsequent design. The middle swing arm, however, bears the primary load during the vehicle posture transformation and obstacle-crossing process. Therefore, its structural strength at the connection points with the frame and the cylinder push rod should be carefully ensured in the optimization design to guarantee the operational safety of the forestry unmanned vehicle.

Introduction to Topology Optimization

The concept of structural topology optimization originated from Michell's study on truss structure design. In the entire design optimization process, it belongs to the conceptual design phase, which determines the design direction. Topology optimization can, based on the given boundary conditions and loading scenarios, find the optimal material distribution or load path within the design space, thus achieving the lightest design while satisfying various performance criteria.

This paper uses the density method for material modeling based on OptiStruct topology optimization *(Tan et al., 2022*). In this method, each element in the finite element model design space is assigned to a relative density ρ_i as an optimization design variable, with a value range of $0 \leq \rho_i \leq 1$. When $\rho_i = 0$, it indicates that material is removed; when $\rho_i = 1$, it indicates that material is retained. This converts the structural topology optimization problem into an optimal material distribution problem, which is solved using mathematical programming methods.

Common material interpolation models in the density method include Solid Isotropic Material with Penalization (SIMP) and Rational Approximation of Material Properties (RAMP) *(Bai et al., 2024; Wang et al., 2021*). The OptiStruct solver uses the SIMP method, which introduces a penalty factor to penalize intermediate density values, causing the density values to converge toward 0 or 1. This results in a clear 0-1 optimization, approximating solid or void material distributions.

Analysis of Typical Swing Arm Loading Conditions

Due to the similar shapes and symmetric structures of the front and rear suspension arms, they can be analyzed together for their loading conditions. By analyzing the unmanned vehicle's movement and obstacle-crossing process, five typical loading conditions for the front/rear swing arms can be identified:

1. Static state loading condition;
2. Obstacle overcoming loading condition;
3. Under electric cylinder action condition;
4. Differential steering condition;
5. Emergency braking condition.

Similarly, five typical loading conditions can be identified for the middle swing arm:

1. Static state loading condition;
2. Arm raised loading condition;
3. Under electric cylinder action condition;
4. Arm returning after crossing obstacle loading condition;
5. Differential steering condition.

The load conditions of differential steering and emergency braking are calculated using the inertia release method (*Huang et al., 2025*), while the load conditions for others are derived from the dynamic simulation results in MSC Adams.

All the load conditions are shown in Table 3, where F_x, F_y, F_z represent the forces in the X, Y, and Z directions. The coordinate system for each axis swing arm is shown in Fig. 5.

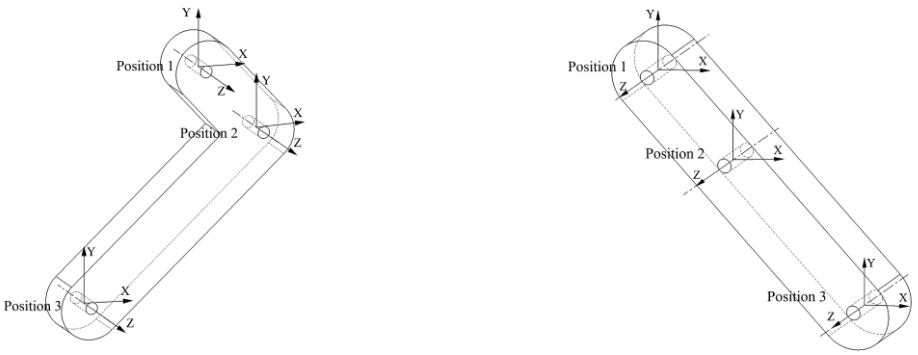

(a) (b)

Fig. 5 - Swing arm coordinate system
(a) Front/rear arm; (b) Middle arm

Table 3

Load conditions for each scenario

Condition	Front/Rear Arm			Middle Arm		
	Position 1	Position 2	Position 3	Position 1	Position 2	Position 3
1	Constrained	$F_y = -4166N$	$F_y = 4166N$	$F_y = -4166N$	Constrained	$F_y = 4166N$
2	$F_x = -9660N$ $F_y = -1700N$ $F_z = 1400N$	Constrained	$F_x = 2167N$ $F_y = 3383N$	$F_x = 1400N$ $F_y = -4200N$ $F_z = 4000N$	Constrained	$F_y = 8000N$
3	$F_x = 9339N$ $F_y = -2550N$ $F_z = 1500N$	Constrained	$F_x = 2200N$ $F_y = 3383N$	Constrained	$F_x = 11000N$ $F_y = 22000N$ $F_z = -4800N$	Constrained
4	Constrained	$F_y = -8333N$ $F_z = -6666N$	$F_y = 8333N$ $F_z = 6666N$	$F_x = 10242N$ $F_y = -12261N$ $F_z = -3900N$	Constrained	$F_y = 9400N$
5	Constrained	$F_x = -12500N$ $F_y = 12500N$	$F_x = 12500N$ $F_y = 12500N$	$F_y = -8177N$ $F_z = -6533N$	Constrained	$F_y = 8177N$ $F_z = 6533N$

Swing Arm Topology Optimization Mathematical Model

In multi-condition continuum structure topology optimization, the weighted compromise programming method is used. Based on the weight coefficients for each condition, the objective function values for each individual condition are linearly weighted, transforming the multi-condition topology optimization problem into a single-condition topology optimization problem (*Guo-fei et al., 2018*). Based on the variable density method, where the relative density of the elements is taken as the design variable, the objective is to minimize the structural compliance (flexibility) under different loading conditions.

The mathematical model for the swing arm's compliance minimization topology optimization under multiple conditions is formulated as follows:

$$\begin{cases} X = (X_1, X_2, \dots, X_n)^T, \min\limits_X C(X) = \sum\limits_{k=1}^{n} \omega_k C_k(X) \\ Subject\ to: \begin{cases} \sum\limits_{i=1}^{n} x_i v_i - f_v V_0 \le 0 \\ 0 < \rho_{min} \le \rho_i \le 1 \\ k = 1,2,\dots,n \end{cases} \end{cases} \quad (1)$$

where X is the relative density of the elements in the design domain, which is the design variable; $C(X)$ is the weighted compliance of the swing arm structure, which is the objective function; $C_k(X)$ is the objective function for the k-th loading condition; ω_k is the weight coefficient for the k -th condition; n is the total number of discrete elements; k is the number of loading conditions; ρ_i is the relative density of the i-th element; v_i is the volume of the i-th element; f_v is the volume fraction corresponding to the volume constraint of the optimization objective; and V_0 is the initial volume.

The Analytic Hierarchy Process (*Kayet et al., 2020*) is used to perform pairwise comparisons of the k conditions and construct a decision matrix to determine the weight coefficient ω_k for each condition. From the mathematical model of compliance minimization, it is clear that the optimal compliance values for the initial topology optimization model under each individual condition determine the corresponding weight coefficients for multi-condition topology optimization. The initial topology optimization model for the swing arm is optimized separately under each condition to obtain the optimal compliance values α_k for each condition, and a decision matrix is then constructed.

$$M = \begin{pmatrix} \frac{\alpha_1}{\alpha_1} & \frac{\alpha_1}{\alpha_2} & \cdots & \frac{\alpha_1}{\alpha_k} \\ \frac{\alpha_2}{\alpha_1} & \frac{\alpha_2}{\alpha_2} & \cdots & \frac{\alpha_2}{\alpha_k} \\ \vdots & \vdots & \ddots & \vdots \\ \frac{\alpha_k}{\alpha_1} & \frac{\alpha_k}{\alpha_2} & \cdots & \frac{\alpha_k}{\alpha_k} \end{pmatrix} \quad (2)$$

The maximum eigenvalue λ_{max} of the decision matrix M is solved, and the corresponding eigenvector $a = [\omega_1, \omega_2, \ldots, \omega_k]$ is obtained. Normalizing the eigenvector gives the weight coefficients ω_k for each condition in the objective function.

Swing Arm Structure Topology Optimization

The profile models of the front, middle, and rear swing arms are created using SolidWorks. Based on the force conditions at key nodes from the dynamic simulation described, the OptiStruct solver on the HyperMesh platform is used to perform topology optimization on the swing arms for each axle.

Considering the interchangeability of the front and rear swing arm structures, the front and rear arm models are combined to improve computational efficiency. Based on the mounting positions of the swing arms, vehicle frame, wheels, and drive cylinder rods, the initial topology optimization models for the front/rear arm and the middle arm are established. The mounting positions of the swing arms on the frame, wheels, and drive cylinder rods are designated as non-design regions. This means that the material in non-design regions is kept fixed during the optimization process, while other regions are designated as design regions.

Fig. 6 shows the initial topology optimization model for the swing arm. Due to its symmetrical shape and relatively regular structure, a 4mm hexahedral element mesh is used for discretization. The parameters for the topology optimization model are listed in Table 4.

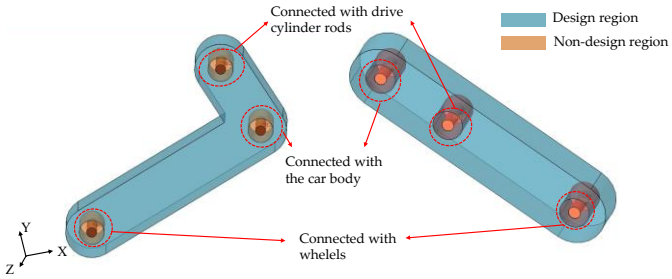

Fig. 6 - Initial topology optimization models for front/rear arm and middle arm

Table 4

Topology optimization model material parameters

Parameter	Value
Material	7A58AL
Density (kg/m^3)	2.78 × 10^3
Young's Modulus (MPa)	6.89 × 10^4
Poisson's Ratio	0.33
Shear modulus (MPa)	2.6 × 10^4
Yield Strength (MPa)	345

The initial topology optimization models for the front/rear arm and the middle arm are optimized individually under five different conditions. The optimal compliance values for the front/rear arm under each condition are denoted as $\alpha_1 = 118979Nmm, \alpha_2 = 361640Nmm, \alpha_3 = 421899Nmm, \alpha_4 = 1200140Nmm$ and $\alpha_5 = 368721Nmm$.

The optimal compliance values for the middle arm under each condition are denoted as $\beta_1 = 374471Nmm, \beta_2 = 1391650N \cdot mm, \beta_3 = 1043790N \cdot mm, \beta_4 = 1001620N \cdot mm$ and $\beta_5 = 2780710N \cdot mm$.

The α values are then used to construct the decision matrix for the topology optimization objective function for the front/rear swing arm.

$$M_1 = \begin{pmatrix} 1.00 & 0.33 & 0.28 & 0.10 & 0.32 \\ 3.04 & 1.00 & 0.86 & 0.30 & 0.98 \\ 3.55 & 1.17 & 1.00 & 0.35 & 1.14 \\ 10.09 & 3032 & 2.84 & 1.00 & 3.26 \\ 3.10 & 1.02 & 0.87 & 0.31 & 1.00 \end{pmatrix} \quad (3)$$

The maximum eigenvalue $\lambda_1 = 5$ of matrix M_1 is solved, and corresponding eigenvector $a_1 = [0.086\ 0.26\ 0.31\ 0.87\ 0.27]$ is obtained. By normalizing the eigenvector, the weight coefficients of the front/rear arm for the five conditions are determined as 0.048, 0.15, 0.17, 0.49, 0.15.

Then the β values are then used to construct the decision matrix for the topology optimization objective function for the middle swing arm.

$$M_1 = \begin{pmatrix} 1.00 & 0.27 & 0.36 & 0.37 & 0.14 \\ 3.72 & 1.00 & 1.33 & 1.39 & 0.50 \\ 2.79 & 0.75 & 1.00 & 1.04 & 0.38 \\ 3.68 & 0.72 & 0.96 & 1.00 & 3.26 \\ 7.43 & 2.00 & 2.67 & 2.78 & 1.00 \end{pmatrix} \quad (4)$$

The maximum eigenvalue $\lambda_2 = 5$ of matrix M_2 is solved, and corresponding eigenvector $a_2 = [0.11\ 0.40\ 0.30\ 0.29\ 0.81]$ is obtained. By normalizing the eigenvector, the weight coefficients of the front/rear arm for the five conditions are determined as 0.06, 0.21, 0.16, 0.15, 0.42.

The mass fraction and weighted strain energy are defined as constraint conditions. The optimized mass of the front/rear swing arm is set to not exceed 30% of the initial model, and the optimized mass of the middle swing arm is set to not exceed 40% of the initial model. Additionally, the maximum stress is limited to 276 MPa, which is 80% of the yield strength of 7A58 aluminum. A symmetry constraint is also applied to the plane. The calculation is performed using the Optistruct solver, and after 40 iterations, the solution converges, yielding the topology optimization results as shown in Fig. 7. The iteration process of the objective function and compliance values under various conditions is shown in Fig. 8.

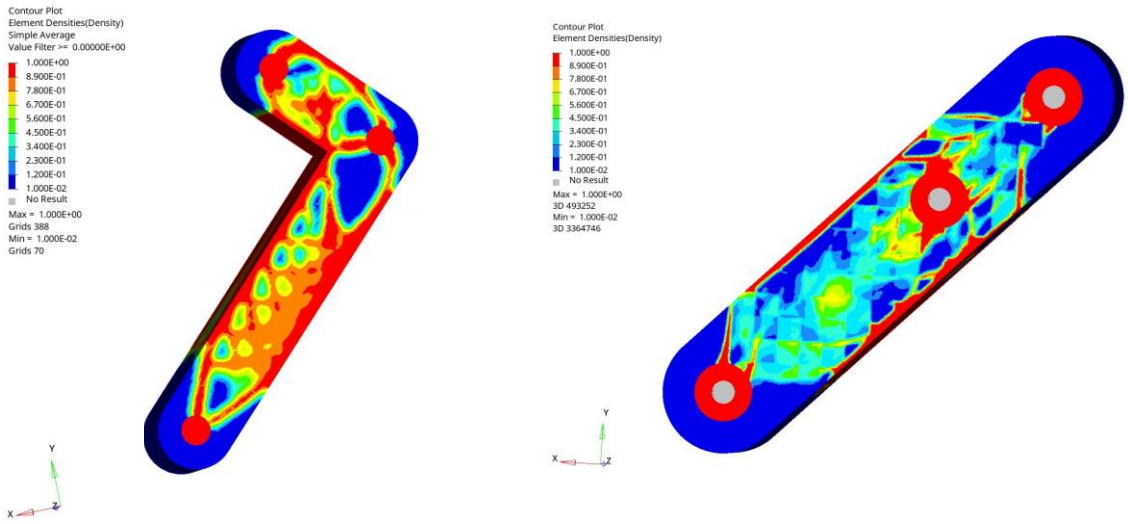

(**a**) (**b**)

Fig. 7 - Topology optimization results for swing arms
(a) Result for the front/rear arm; (b) Result for the middle arm.

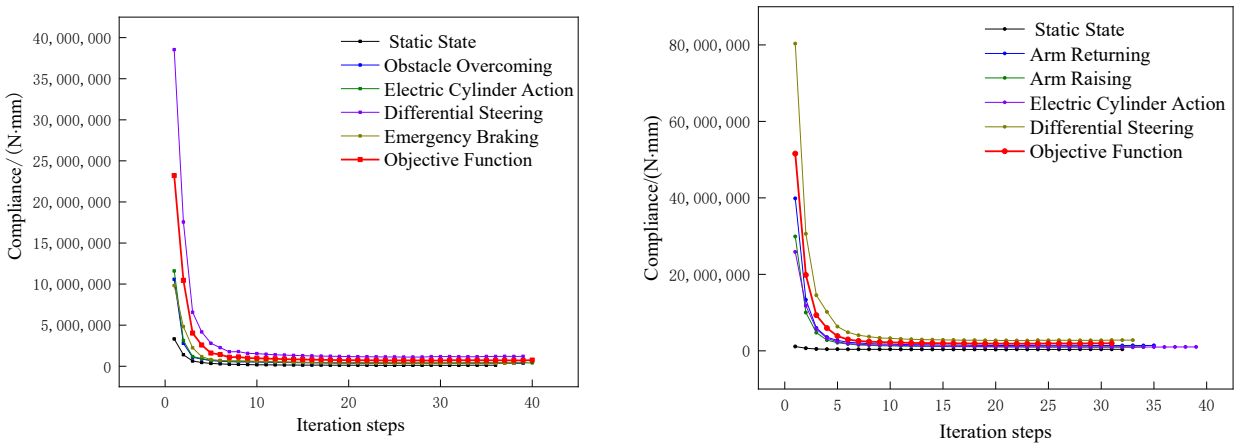

(**a**) (**b**)

Fig. 8 - Objective function and compliance iteration process of each loading condition

(a) Compliance iteration process of the front/rear arm. (b) Compliance iteration process of the middle arm.

Based on the results of the swing arm multi-condition topology optimization, the swing arm structure is geometrically reconstructed. The reconstruction process is divided into the following three steps:

1. Retain the main structural features as much as possible to obtain the external shape of the structure;
2. Weight reduction is primarily applied to the outer sides of the front/rear arms, while retaining a solid structure in the middle. For the middle arm, additional cover plates are added to both outer sides to prevent foreign objects from getting trapped inside the arm during vehicle operation;
3. The middle swing arm should ensure sufficient strength at the middle and both ends where it connects to other structures.

The final geometric models of the swing arms for each axis are shown in Fig. 9.

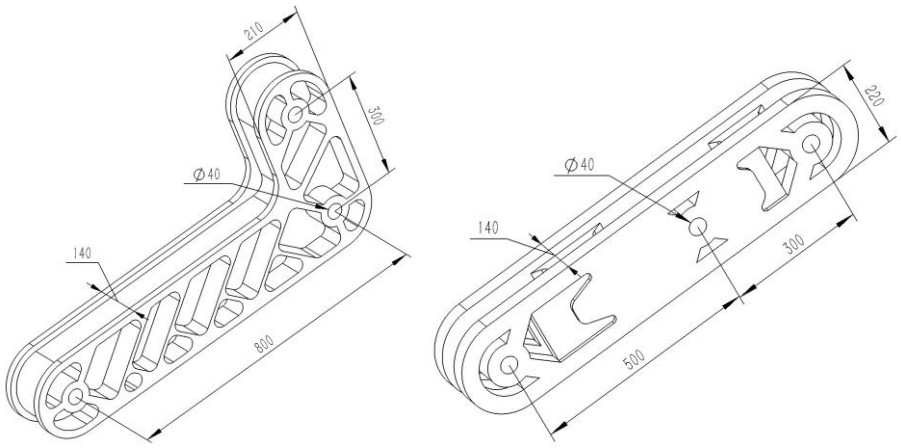

Fig. 9 - Reconstructed geometric models of the swing arms

Performance Verification of the Optimized Swing Arm Model

To verify whether the performance of the swing arms after topology optimization meets the requirements, a performance check is conducted on the optimized swing arm model. In HyperMesh software, a tetrahedral mesh with a size of 4 mm is used for discretization. Constraints are applied to the connection holes using RBE2 elements, and the load application positions are defined with RBE3 elements. The constraint conditions corresponding to the five scenarios are the same as those in Table 3 and the finite element model is illustrated in the Fig 10.

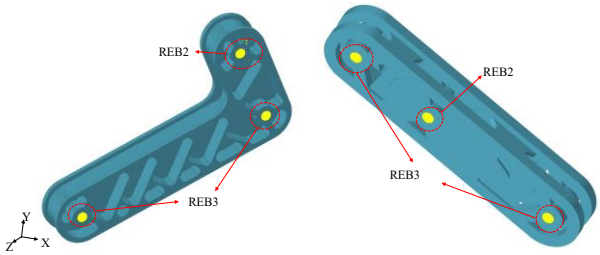

Fig. 10 - Finite element models of the swing arms

The calculations are performed using the OptiStruct solver, and stress contour maps for the swing arms under each condition are shown in Fig.11 and Fig.12. Table 4 summarizes the specific stress distribution.

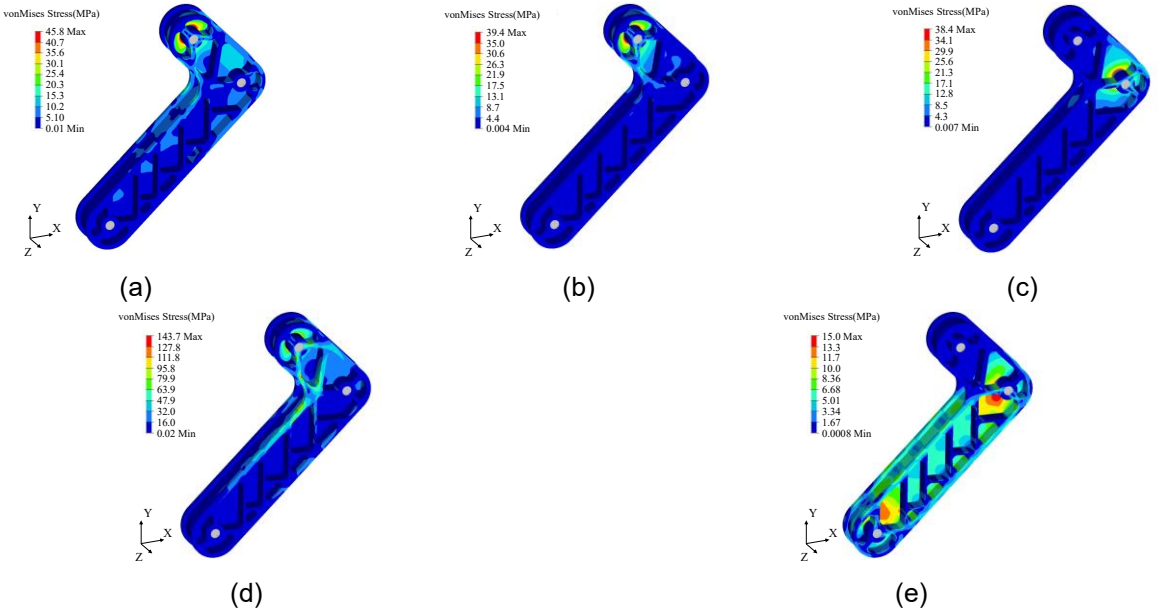

Fig. 11 - Stress contour map of the front/rear arm under five loading conditions

*(**a**) Static state loading condition; (**b**) Obstacle overcoming condition; (**c**) Electric cylinder action condition; (**d**) Differential steering condition; (**e**) Emergency braking condition.*

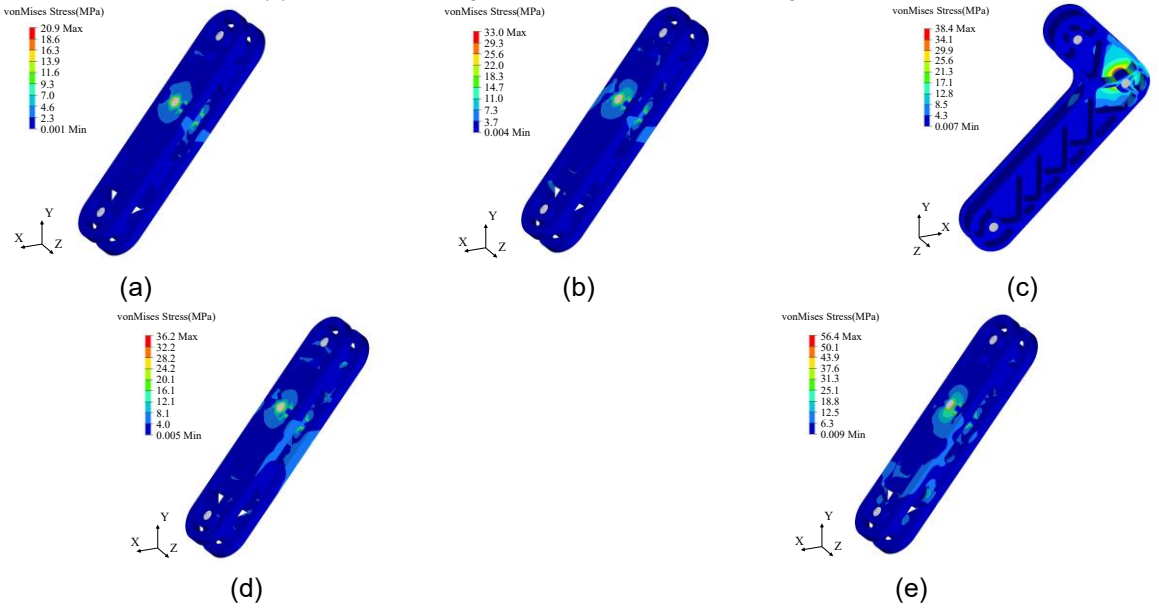

Fig. 12 - Stress contour map of the middle arm under five loading conditions

*(**a**) Static state loading condition; (**b**) Arm raised loading condition; (**c**) Electric cylinder action condition; (**d**) Arm returning condition; (**e**) Differential steering condition.*

Table 5

Maximum stress of the swing arms for each axle under five conditions

Condition	Maximum stress of the front/rear arm (MPa)	Maximum stress of the middle arm (MPa)
1	45.8	20.9
2	39.4	33.0
3	38.4	25.9
4	143.7	36.2
5	15.0	56.4

It is clearly shown in Table 5 that the maximum stresses for the two types of swing arms under five typical working conditions are 143.7 MPa and 56.41 MPa. These maximum stresses are mainly located at the connection points between the swing arms of each axle and the cylinder push rod under steering conditions, which account for 41.65% and 16.35% of the maximum allowable stress, respectively. Considering the possibility of extreme working conditions, the minimum safety factor of the swing arms is set around 2.4. Through finite element mesh calculations, the optimized weights are 31.3 kg for the front/rear swing arms and 39.44 kg for the middle swing arm. In comparison to the initial model weights of 44.12 kg and 49.47 kg for the swing arms, the weight reduction rates are 29.1% and 20.28%.

RESULTS

Experimental Verification and Results Analysis of the Aluminum Swing Arms Specimen

Due to the high manufacturing costs of the unmanned vehicle swing arms and frame, along with limitations in testing conditions, performing an aluminum alloy swing arm test that simulates real-world operational conditions is very challenging. Therefore, the tests in this paper, within the allowed conditions, include free vibration modal testing and static mechanical testing under bending conditions for each axle of the swing arm. While these tests cannot fully represent the actual working conditions of the swing arm, they provide valuable experimental data on the mechanical behavior and response of aluminum alloy swing arms. This data can be compared and evaluated against finite element analysis results to verify the accuracy of the finite element analysis and provide insights and directions for future research.

Modal Testing

Modal testing is a method used to determine the inherent characteristics of a vibrating system. The goal is to obtain the system's modal parameters, including natural frequency, damping ratio, vibration modes, and modal mass, all of which describe the intrinsic properties of the system in the frequency domain. Through vibration modal analysis, the natural vibration modes of the structure can be revealed, helping to identify potential vibration issues, fatigue life, and structural safety (*Qingge et al., 2025*). Additionally, vibration modal analysis serves as a basis for structural health monitoring, fault detection, and prediction (*Zou et al., 2023*).

In the vibration modal test of the swing arm, the DH5922N dynamic signal testing system is used for precise measurement and analysis. This system can accurately record and analyze the vibration response of the swing arm under hammer impact excitation. By applying impact excitation at different positions and recording the corresponding vibration signals, the vibration modes of the swing arm at different frequencies can be obtained. These vibration modes include the natural frequencies and vibration shapes of free vibrations, revealing the structural characteristics and vibration behavior of the swing arm.

Before the test begins, as shown in Fig 13 above, elastic cords are tied to both ends of the swing arm and suspended from a load-bearing frame, allowing the swing arm to be in a free-floating state to ensure its free modal condition.

(**a**) (**b**) (**c**)

Fig. 13 - Modal test photographs

(a) Test for front/rear arm; (b) Test for middle arm; (c) DH5922N Dynamic Signal Testing and Analysis System.

It is important to ensure that the distance between the swing points of the swing arm and the elastic cords is sufficiently large to reduce the impact of the increased stiffness caused by tightening the elastic cords, thus improving the accuracy of the test results. The DH5922N system establishes a connection with the swing arm through a piezoelectric velocity sensor. A force hammer is used to strike the swing arm to induce vibration and excite its natural frequency. Through the system's data acquisition function, the time-domain signal of the swing arm's vibration is recorded in real time. A Fast Fourier Transform (FFT) is then performed to convert the time-domain signal into a frequency-domain signal (*Chen & Li, 2019*), from which the peak values of the frequency-domain signal are extracted, representing the natural frequencies of the swing arm, as shown in Fig.14.

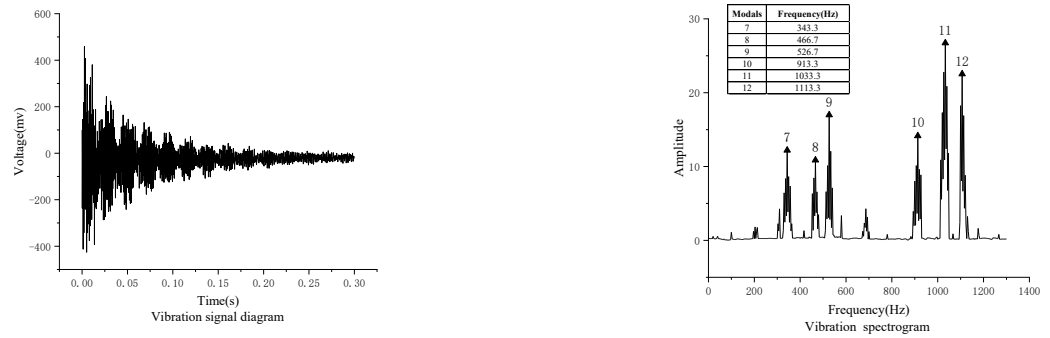

(**a**)

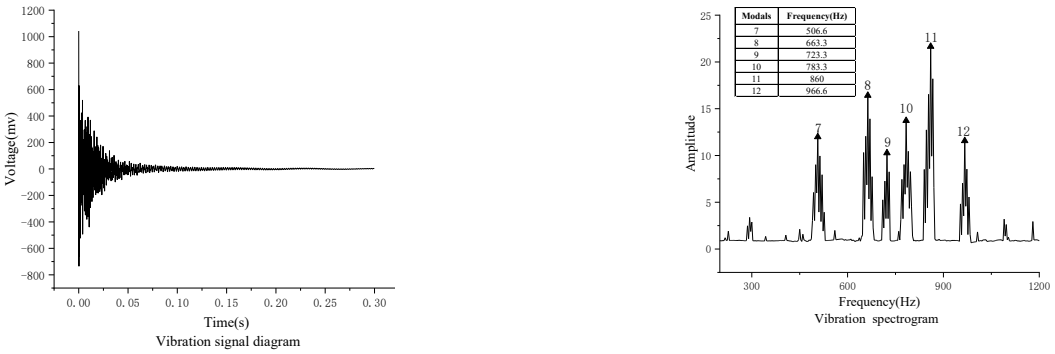

(**b**)

Fig. 14 - Modal test results of each axle swing arm

(a) Front/rear arm; (b) Middle arm.

After the test, a finite element model of the swing arm specimen was established, and a 12-order vibration modal analysis was conducted. Since the first six modes are rigid body vibration modes, only the 7th to 12th modes are shown. The vibration mod-al frequencies obtained from the test were compared with the finite element simulation results under the same test conditions, and the specific results are shown in Table 6.

The results indicate that the relative error between the two for each mode is less than 10%, demonstrating that the modal analysis process of the finite element model closely fits the actual test data.

Table 6

Maximum stress of the swing arms for each axle under five conditions

Modals	Front/Rear Arm			Middle Arm		
	Calculated Frequency (Hz)	Experimental Frequency (Hz)	Relative Error	Calculated Frequency (Hz)	Experimental Frequency (Hz)	Relative Error
7	344.7	343.3	0.41%	508.4	506.6	0.35%
8	459.3	466.7	-1.61%	730.6	663.3	9.21%
9	513.1	526.7	-2.65%	732.0	723.3	1.19%
10	973.1	913.3	6.15%	864.1	783.3	9.35%
11	1040.6	1033.3	0.70%	887.6	860	3.11%
12	1055.1	1113.3	-5.52%	895.9	966.6	-7.89%

The modal analysis results show that the 7th vibration mode frequencies of the swing arms for each axle are 344.7 Hz and 508.4 Hz, respectively. Under normal conditions, the road surface excitation frequency is typically up to 28 Hz, while the hub motor excitation frequency ranges from 50-60 Hz (*Zhang et al., 2019*). Since the natural frequencies of the swing arms are much higher than the upper limit of their excitation frequencies, it can be confirmed that resonance will not occur between the two.

Static Testing

Due to testing constraints, it was not possible to simulate the actual motion conditions of the swing arms. Therefore, a simple bending condition was designed, where the upper end of the swing arm is fixed, and a load is applied at the lower end. This condition has simple boundary constraints, making the experiment easier to control and measure, which improves the repeatability and accuracy of the test, thereby better verifying the rationality of the finite element analysis. The strain of the specimen under static load conditions is precisely measured using the resistance method.

After establishing the finite element model for the swing arm, strain gauges were applied at the locations where stress verification was required, based on the stress contour maps. On the test bench, the swing arm specimen's top and middle were fixed by locking the angle of the electric cylinder and the cylinder rod length, while the load was applied at the bottom of the specimen using standard weight blocks, simulating the constraints and loads from the static analysis. The specific locations for strain gauge application, fixation, and loading are shown in Fig. 15 and Fig. 16.

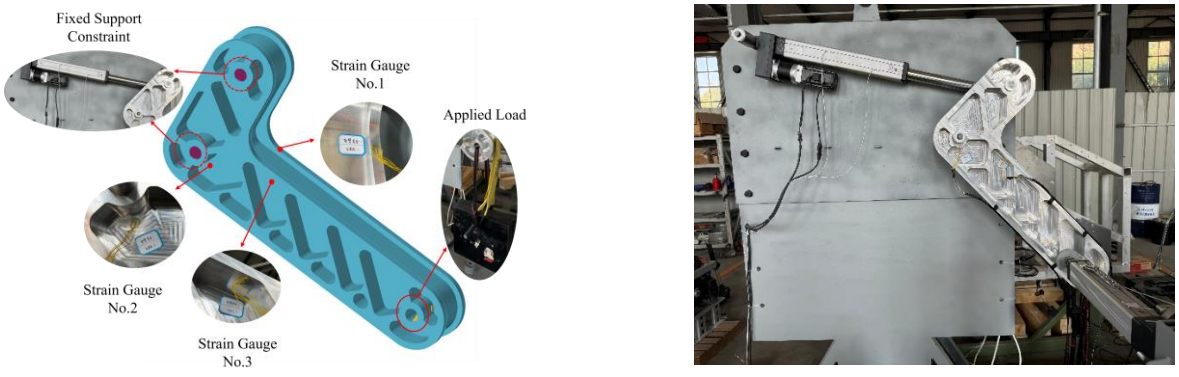

Fig. 15. Static test of front/rear arm specimen

(a) Strain gauges placement locations for swing arm specimen stress test; (b) Static test photograph.

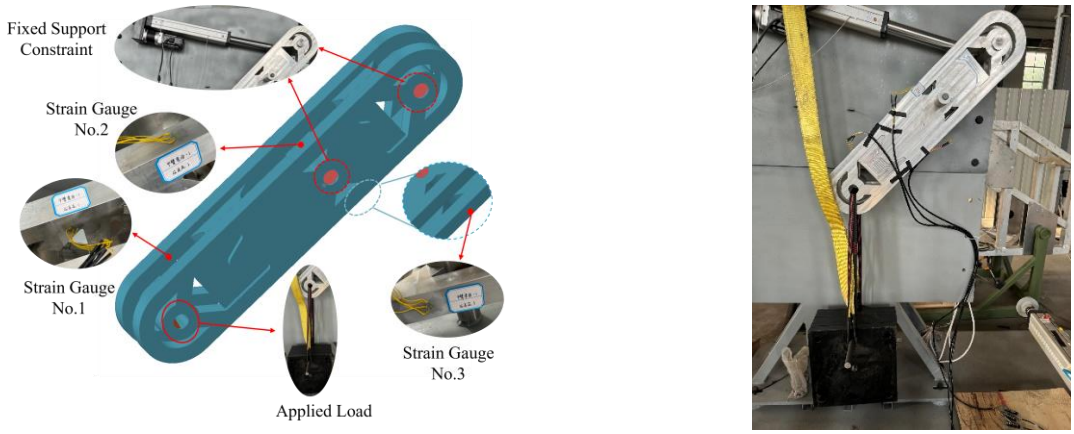

(a) **(b)**

Fig. 16 - Static test of middle arm specimen

*(**a**) Strain gauges placement locations for swing arm specimen stress test; (**b**) Static test photograph.*

Strain gauges at each measurement location were connected to the DH5922N system via a strain indicator, measuring the strain in three directions: $\varepsilon_{0°}$, $\varepsilon_{45°}$ and $\varepsilon_{90°}$. To minimize errors, the specimen underwent three test trials. After the tests, the measured strain values were exported and substituted into the following formula to calculate the von Mises stress for each strain gauge location (*Chen et al., 2025*).

$$\sigma = \frac{E(\varepsilon_{0°} - \varepsilon_{90°})}{2(1-\mu)} + \frac{\sqrt{(\varepsilon_{0°} - \varepsilon_{45°})^2 + 2(\varepsilon_{45°} - \varepsilon_{90°})^2}}{\sqrt{2}(1+\mu)} \quad (5)$$

The von Mises stress results from the finite element model at corresponding locations in HyperView were compared with the experimental data, as shown in Table 7.

Table 7

Comparison of static test results for each axle swing arm specimen

Arm Specimen	Strain Gauge Number	Applied load (N)	Calculated Stress (MPa)	Experimental Stress (MPa)	Relative Error
Front/Rear	1-1	1500	5.64	5.38	-4.61%
Front/Rear	1-2	1500	3.42	3.23	-5.56%
Front/Rear	1-3	1500	4.25	4.03	-5.18%
Front/Rear	2-1	2500	9.39	9.55	1.70%
Front/Rear	2-2	2500	5.7	6.11	7.19%
Front/Rear	2-3	2500	7.08	7.35	3.81%
Middle	1-1	1500	1.06	1.02	-3.77%
Middle	1-2	1500	0.91	0.95	4.40%
Middle	1-3	1500	0.84	0.81	-3.57%
Middle	2-1	2500	1.67	1.61	-3.59%
Middle	2-2	2500	1.52	1.59	4.61%
Middle	2-3	2500	1.41	1.51	7.09%

The test results show that the maximum relative error between the stress calculated by finite element analysis and the test stress is 7.19%, indicating that the accuracy of the static analysis process in the finite element model is relatively high.

CONCLUSIONS

This paper presents the design of a tri-axle unmanned vehicle with a swing arm and wheel-leg hybrid configuration, optimized for excellent obstacle-crossing performance under forestry production site conditions. After conducting dynamic simulations to obtain the different loading conditions for the swing arms, optimization was per-formed. Using the Analytic Hierarchy Process (AHP), the five typical loading conditions of the swing arms were weighted and analyzed. The swing arms were then subjected to multi-condition topology optimization and lightweight design using the Hypermesh-Optistruct software. The optimized mass of the front/rear swing arms and the middle swing arm are 31.3 kg and 39.44 kg, respectively, with weight reduction rates of 29.1% and 20.27%, meeting the lightweight requirements.

Static and vibration modal tests were conducted on the processed swing arm specimens, verifying the effectiveness and accuracy of the finite element analysis. The relevant conclusions of this study provide valuable references for the topology optimization and lightweight design of the continuous body structure of forestry unmanned vehicles.

ACKNOWLEDGEMENT

The authors were funded for this project by the National Natural Science Foundation of China (NSFC) (No.51475255).

REFERENCES

[1] Bai, H., Xing, P.-f., & Wu, M.-w. (2024). Research on Topology Optimization and Lightweight Design of Continuum Structures under Multiple Serving Conditions (连续体结构多工况拓扑优化与轻量化设计研究). *Tractor & Farm Transporter*, *51*(2), 76-83.

[2] Chen, G., & Li, X. (2019). Modal analysis on the linear module with ball screw (滚珠丝杠直线模组的模态分析). *Journal of Machine Design*, *36*(03), 56-61. https://doi.org/10.13841/j.cnki.jxsj.2019.03.010

[3] Chen, Q., Zhao, Y., Wang, D., Chen, Z., Wang, Q., & Yuan, X. (2025). Multi-Level Matching Optimization Design of Thin-Walled Beam Cross-Section for Tri-Axle Unmanned Forestry Vehicle Frame. *Forests*, *16*(1), 69. https://doi.org/10.3390/f16010069

[4] Chen, Y., Zhu, J., Yao, L., Yang, Z., Hu, Z., Xu, L., & Yao, L. (2024). Analysis and Optimization of Driving Performance for Tree Transplanting Machine in Hilly Mountainous Areas. *Forests*, *15*(12). https://doi.org/10.3390/f15122128

[5] Chenwei, H., Jiayu, C., Yu, C., & Liquan, L. (2023). Design and Analysis of Independent Strut Type Air Suspension Applied to High Clearance Self-Propelled Sprayer (应用于高地隙自走式喷雾机的独立式立轴空气悬架设计与分析). *INMATEH-Agricultural Engineering*, *71*(3). https://doi.org/10.35633/inmateh-71-04

[6] Guo-fei, Y., Hai-bing, W., Fei, H., & Zhong-wu, W. (2018). Topology Optimization Design with the Globalization of Stress Constrains and Analytic Hierarchy Process (结合应力全局化与层次分析的拓扑优化设计). *Machinery Design & Manufacture*(06), 200-202+206. https://doi.org/10.19356/j.cnki.1001-3997.2018.06.053

[7] Huaitang, Z., Zilong, D., Tiemin, G., & Yan, H. (2024). Dynamics Simulation Analysis on Configuration Change of Metamorphic Lifting Mechanism Based on ADAMS(基于 ADAMS 变胞升降机构构态变换动力学仿真分析). *Journal of Liaoning University of Petroleum & Chemical Technology*, *44*(4), 60. https://doi.org/10.12422/j.issn.1672-6952.2024.04.008

[8] Huang, Y., Peng, W., Li, H., Lin, L., Shao, Y., & Shen, H. (2025). Finite Element Analysis of Structural Strength of Complex Aluminum Alloy Knuckle Under Multiple Working Conditions and Load Channels (多载荷通道复杂铝合金转向节的多工况结构强度有限元分析). *Mechanical Science and Technology for Aerospace Engineering*, *44*(5), 857-867. https://doi.org/10.13433/j.cnki.1003-8728.20230230

[9] Jing-liang, W., Tian-cheng, Z., Long-biao, Z., & Fei-yun, X. (2022). Research on variable density topology optimization method for continuum structure (连续体结构的变密度拓扑优化方法研究). *Chinese Journal of Engineering Design*, *29*(3), 279-285. https://doi.org/https://doi.org/10.3785/j.issn.1006-754X.2022.00.039

[10] Kayet, N., Chakrabarty, A., Pathak, K., Sahoo, S., Dutta, T., & Hatai, B. K. (2020). Comparative analysis of multi-criteria probabilistic FR and AHP models for forest fire risk (FFR) mapping in Melghat Tiger Reserve (MTR) forest. *Journal of forestry research*, *31*(2), 565-579. https://doi.org/10.1007/s11676-018-0826-z

[11] Kešner, A., Chotěborský, R., Linda, M., Hromasová, M., Katinas, E., & Sutanto, H. (2021). Stress distribution on a soil tillage machine frame segment with a chisel shank simulated using discrete element and finite element methods and validate by experiment. *Biosystems Engineering*, *209*, 125-138. https://doi.org/10.1016/j.biosystemseng.2021.06.012

[12] Li, Y., Chang, T., Kong, W., Wu, F., & Kong, X. (2023). Topological Optimization of Bi-Directional Progressive Structures with Dynamic Stress Constraints under Aperiodic Load. *Applied Sciences*, *14*(1), 322. https://doi.org/10.3390/app14010322

[13] Liu, L. (2020). Design and servo characteristics of two-dimensional turntable(二维转台设计和伺服特性研究) [masters, Chengdu University of Technology]. https://doi.org/10.26986/d.cnki.gcdlc.2020.000529

[14] Meng, Z., Pang, Y., Pu, Y., & Wang, X. (2020). New hybrid reliability-based topology optimization method combining fuzzy and probabilistic models for handling epistemic and aleatory uncertainties. *Computer Methods in Applied Mechanics and Engineering*, *363*, 112886. https://doi.org/10.1016/j.cma.2020.112886

[15] Mergl, V., & Kašpárek, J. (2022). Verifying the Lifting and Slewing Dynamics of a Harvester Crane with Possible Levelling When Operating on Sloping Grounds. *Forests*, *13*(2). https://doi.org/10.3390/f13020357

[16] Niu, Z., Xu, Z., Deng, J., Zhang, J., Pan, S., & Mu, H. (2022). Optimal vibration parameters for olive harvesting from finite element analysis and vibration tests. *Biosystems Engineering*, *215*, 228-238. https://doi.org/10.1016/j.biosystemseng.2022.01.002

[17] Padhi, A. P., Chakraborty, S., Chakrabarti, A., & Chowdhury, R. (2024). Deep learning accelerated efficient framework for topology optimization. *Engineering Applications of Artificial Intelligence*, *133*, 108559. https://doi.org/10.1016/j.engappai.2024.108559

[18] Qiang, G., Jian, W., Yan, Z., Xuyang, Z., LÜ Hao, & Guodong, Y. (2024). Topology Optimization Approaches and Its Application and Prospect in Transportation Engineering (拓扑优化方法及其在运载工程中的应用与展望). *Journal of Mechanical Engineering*, *60*(4), 369-390. https://doi.org/10.3901/jme.2024.04.369

[19] Qingge, L., Haitao, L., Fengxia, H., Yuxin, L., & Yanbin, L. (2025). Model test and dynamic similarity study of large space truss structure (空间大型桁架结构模型试验与动力相似研究). *Manufacturing Technology & Machine Tool,* (01), 33-40. https://doi.org/10.19287/j.mtmt.1005-2402.2025.01.005

[20] Qiu, C., Du, S., & Yang, J. (2021). A deep learning approach for efficient topology optimization based on the element removal strategy. *Materials & Design*, *212*, 110179. https://doi.org/10.1016/j.matdes.2021.110179

[21] Sun, S., Zhang, S., Li, Y., Wu, J., & Chu, J. (2019). Studies of several large-scale forestry operating vehicles at home and abroad and prospect of vehicle type design(国内外林区几种大型作业车辆研究进展及车型设计展望). *Journal of Beijing Forestry University*, *41*(6), 154-166. https://doi.org/10.13332/j.1000-1522.20190048

[22] Tan, L., Cheng, B., Jia, D., & Gao, D.-w. (2022). Topology Optimization Design of an Aeroengine Bracket under Multiple Load Cases (多工况下的发动机支架拓扑优化设计). *Aeroengine*(2), 90-95. https://doi.org/10.13477/j.cnki.aeroengine.2022.02.013

[23] Wang, C., Li, M., Cheng, A., He, Z., & Yu, W. (2024). Lightweight Design of Material-Structure for Steel-Aluminum Hybrid Cab (钢-铝混合驾驶室材料-结构轻量化设计). *Automotive Engineering*, *46*(4), 735-744. https://doi.org/10.19562/j.chinasae.qcgc.2024.04.019

[24] Wang, X., Liu, H., Kang, Z., Long, K., & Meng, Z. (2021). Topology optimization for minimum stress design with embedded movable holes. *Computers & structures*, *244*, 106455. https://doi.org/10.1016/j.compstruc.2020.106455

[25] Wang, Y., Tan, X., Ban, X., Li, D., & Yue, S. (2024). Research on a wheel-legged obstacle-crossing robot (一种轮腿式越障机器人的研究) [J]. *Journal of Mechanical Transmission*, *48*(01), 128-134. https://doi.org/10.16578/j.issn.1004.2539.2024.01.019

[26] Wentao, X., Lei, H., Yanhua, M., Tao, L., & Wen, L. (2025). Design and Experimental Study of a High Ground Clearance Weeding Robot Chassis (高地隙跨垄除草机器人底盘设计与试验). *INMATEH-Agricultural Engineering*, *75*(1). https://doi.org/https://doi.org/10.35633/inmateh-75-93

[27] Xia, H., & Qiu, Z. (2022). An efficient sequential strategy for non-probabilistic reliability-based topology optimization (NRBTO) of continuum structures with stress constraints. *Applied Mathematical Modelling*, *110*, 723-747. https://doi.org/10.1016/j.apm.2022.06.021

[28] Xiaokai, C., Chao, L., Yingchun, B., & Zifa, Y. (2021). Multi-material Topology Optimization of Automotive Control Arm(汽车多材料控制臂拓扑优化方法). *Automotive Engineering 43*(07), 1088-1095. https://doi.org/10.19562/j.chinasae.qcgc.2021.07.016

[29] Xiong, F., Wang, D., Ma, Z., Chen, S., Lv, T., & Lu, F. (2018). Structure-material integrated multi-objective lightweight design of the front end structure of automobile body. *Structural and Multidisciplinary Optimization*, *57*(2), 829-847. https://doi.org/10.1007/s00158-017-1778-1

[30] Zhang, J., Chen, K., & Dai, Y. (2019). Design and Modal Analysis of Electric Vehicle Frame for Modern Agricultural Manor (面向现代农业庄园的电动车车架设计及模态分析). *Journal of Chinese Agricultural Mechanization*, *40*(2), 109-112. https://doi.org/10.13733/j.jcam.issn.2095-5553.2019.02.17

[31] Zhang, K., LI, S., & Sun, M. (2020). Lightweight optimization design of commercial vehicle frames combined by steel and aluminum materials under multiple working conditions (钢铝材料结合的商用车车架多工况轻量化优化设计). *China Mechanical Engineering*, *31*(18), 2206.

[32] Zhao, X., Zhao, J., Zhao, J., Ma, Z., Li, J., Dai, B., An, M., Wang, J., & Hao, J. (2025). Optimisation design and experimental analysis of rotary blade reinforcing ribs using DEM-FEM techniques. *Biosystems Engineering*, *249*, 1-17. https://doi.org/10.1016/j.biosystemseng.2024.11.015

[33] Zou, X., Gou, L., Fu, L., Jiang, H., & Liu, L. (2023). Finite Element Analysis and Lightweight Design of the Lower Control Arm for All-Terrain Vehicle Suspension (全域车悬架下控制臂有限元分析及轻量化设计). *Journal of Highway and Transportation Research and Development*, *40*(12), 227-235. https://doi.org/10.3969/j.issn.1002-0268.2023.12.026